Advanced three-dimensional electron microscopy techniques in the quest for better structural and functional materials

2013 Sci. Technol. Adv. Mater. 14 014206

(http://iopscience.iop.org/1468-6996/14/1/014206)

OPEN ACCESS
IOP PUBLISHING
SCIENCE AND TECHNOLOGY OF ADVANCED MATERIALS
Sci. Technol. Adv. Mater. **14** (2013) 014206 (13pp)
doi:10.1088/1468-6996/14/1/014206

Advanced three-dimensional electron microscopy techniques in the quest for better structural and functional materials

D Schryvers, S Cao[1], W Tirry[2], H Idrissi and S Van Aert

EMAT, University of Antwerp, Groenenborgerlaan 171, B-2020 Antwerp, Belgium

E-mail: nick.schryvers@ua.ac.be

Received 27 August 2012
Accepted for publication 19 November 2012
Published 13 March 2013
Online at stacks.iop.org/STAM/14/014206

Abstract
After a short review of electron tomography techniques for materials science, this overview will cover some recent results on different shape memory and nanostructured metallic systems obtained by various three-dimensional (3D) electron imaging techniques. In binary Ni–Ti, the 3D morphology and distribution of Ni_4Ti_3 precipitates are investigated by using FIB/SEM slice-and-view yielding 3D data stacks. Different quantification techniques will be presented including the principal ellipsoid for a given precipitate, shape classification following a Zingg scheme, particle distribution function, distance transform and water penetration. The latter is a novel approach to quantifying the expected matrix transformation in between the precipitates. The different samples investigated include a single crystal annealed with and without compression yielding layered and autocatalytic precipitation, respectively, and a polycrystal revealing different densities and sizes of the precipitates resulting in a multistage transformation process. Electron tomography was used to understand the interaction between focused ion beam-induced Frank loops and long dislocation structures in nanobeams of Al exhibiting special mechanical behaviour measured by on-chip deposition. Atomic resolution electron tomography is demonstrated on Ag nanoparticles in an Al matrix.

Keywords: electron tomography, slice-and-view, Ni–Ti, precipitation, nanomechanics, atomic resolution

1. Introduction

During the last decade, electron microscopes have matured into true measuring devices of the atomic scale, allowing researchers not only to obtain high-quality images of nano- and microscopic features in a given material but also to provide statistically sound numbers of, e.g., particle distributions, local lattice strains, etc, even including atomic positions and shifts down to the picometer scale. In most cases, these evolutions have taken place on the typical two-dimensional (2D) information from scanning or transmission electron microscopy (SEM–TEM) images, but more recently the step towards retrieving quantitative three-dimensional (3D) data from sets of electron microscopy images has been made. The dimensional limitations of 2D microscopy can be overcome by combining a, usually large, set of related 2D images into a 3D data stack. The difference between scanning and transmission EM is expressed in the use of sequential milling and imaging, the so-called slice-and-view technique, in the former and rotational projections for the latter. The final 3D information is retrieved using reconstruction algorithms of different kinds.

Electron tomography in the TEM was first developed and used for decades in the field of biology for solving

[1] Now at Department of Metallic Materials Science & Engineering, South China University of Technology (SCUT), Guangzhou, Wushan 510640, People's Republic of China.
[2] Now at AtlasCopco, Aartselaar, Belgium.

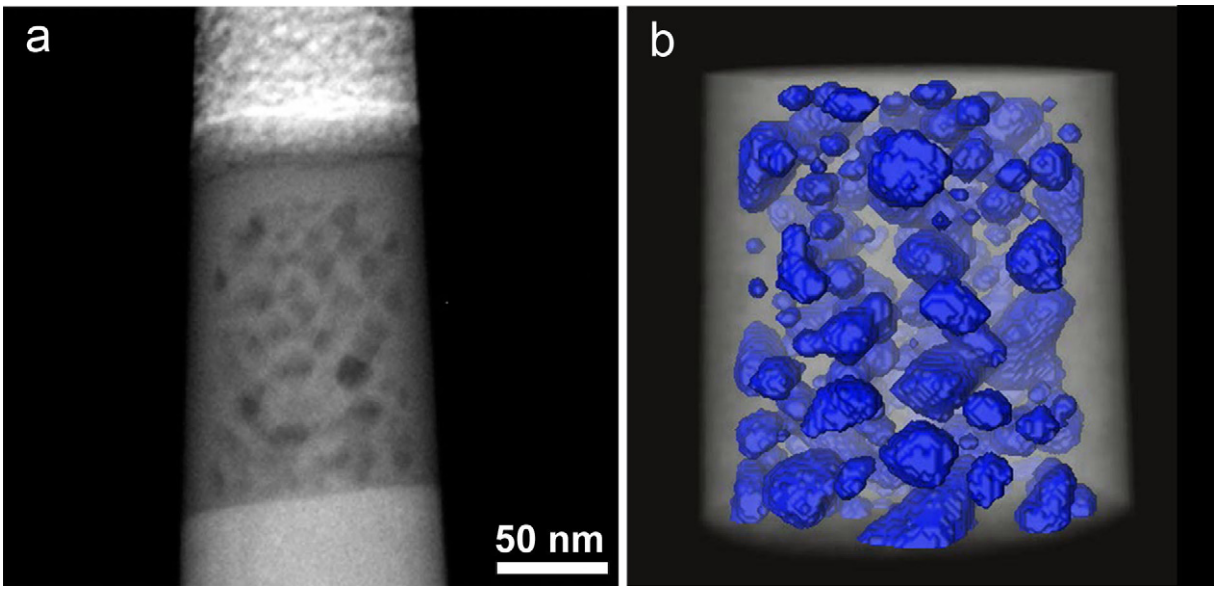

Figure 1. (a) 2D projection image of a needle-shaped pillar of a porous $La_2Zr_2O_7$ layer. (b) Visualization of the 3D SIRT reconstruction showing the pores in dark blue (after figures 1 and 2 of [7]).

morphologies or structures of, e.g., cells, macromolecules, etc, often under cryo conditions (for a review, see, e.g., [1]). The need for each image to be a monotonic projection of a given property of the sample [2] indeed favours amplitude contrast images resulting from, e.g., density fluctuations, as is often the case in life science samples. The strong scattering and contribution of Bragg scattering, which violates this projection requirement in solid crystalline samples, has long inhibited the application of electron tomography in materials science. A little over a decade ago, however, it was demonstrated that high-angle annular dark field (HAADF) scanning transmission electron microscopy (STEM) images as well as energy filtered TEM (EFTEM) maps indeed comply with the projection requirement and that they can thus be used to obtain proper electron tomography series on solid materials [3, 4].

Obtaining 3D information in TEM instruments implies recording a series of images, usually at different tilt angles, aligning the images and applying a well-chosen algorithm, suitable for the research question at hand, to yield a 3D reconstructed volume. In conventional approaches, aiming at visualization of shapes, the number of images in the series, which is mainly determined by the stability of the sample and the design of the holder, determines the quality of the reconstruction. The most important artefact is the so-called missing wedge, severely limiting the resolution along certain viewing directions; this arises from an often limited tilt range due to particular geometries of the tomography holder inside the microscope [3]. The latter can be overcome by using dual-axis holders or needle-shaped samples, the latter usually prepared by a focused ion beam (FIB), allowing for a larger, respectively, full tilt range [5, 6]. An example of the latter is shown in figure 1 obtained from a needle-shaped pillar and revealing the 3D morphology of voids in a porous layer of $La_2Zr_2O_7$ obtained using the simultaneous iterative reconstructive technique (SIRT) [7]. Conversely, shapes and facets of small particles can be investigated, possible even as *in situ* experiments [8].

In novel approaches, often aiming at obtaining quantitative data from the 3D reconstruction, the reconstruction algorithm becomes increasingly important. Before actual reconstruction a segmentation of the grey-scale images is required for proper interpretation and quantification of the pixel content. Manual segmentation is very time consuming and is hampered by subjective interpretation of the images. Therefore, new procedures, often using additional information on the system, have recently been developed. An example of the latter is discrete tomography assuming that the images consist of a limited number of grey scales, which can strongly reduce missing wedge artefacts [9–11]. The ultimate goal is atomic resolution tomography from which atom counts become possible, based on the prior knowledge that the crystal consists of a limited number of specified atoms [12]. An example of the latter for an Ag nano-particle inside an Al matrix is presented in [13] chapter 3.3.

In the SEM the quest for 3D information on internal structures and morphologies has received a serious boost with the appearance of the dual-beam FIB/SEM systems. In this technique, the bulk sample is sliced by the Ga^+ beam of the FIB and SEM images of each fresh surface are obtained using different possible imaging modes [14–18]. In this case, the sectioning parameters, such as the distance between two subsequent cuts rather than the SEM image resolution, determine the quality of the final data. The reconstruction is now a concatenation of all aligned images usually preceded by segmentation to limit the number of grey scales and taking into account the slicing distance (i.e. the amount of lost material due to the Ga^+ sectioning) [14, 16]. In the examples presented below, the technical specifications for selected experiments are given.

The same concept can be used in TEM applying the reduced depth-of-focus in aberration-corrected

HAADF-STEM imaging. Depending on the convergence angle and defocus, very thin slices of the sample are in focus at one given instance, similar to confocal optical microscopy [19]. This so-called optical-depth sectioning allows for atomic resolution in each image and thus in the entire 3D volume, although a strong elongation effect along the electron beam still limits the resolution in this direction [20]. Theoretical simulations indicate that energy filtered scanning confocal EM in combination with chromatic aberration correction may be the most promising technique for resolving this issue [20–23].

At present, many different applications of SEM and TEM tomography exist, often combining different imaging and spectroscopy techniques. For example, dark-field TEM imaging has been used to reconstruct the 3D network of dislocations in GaN [24] and the 3D morphology of secondary γ precipitates together with the compositional distribution in the phase-separated microstructure in a Ni-based superalloy (Ni–8.5 at.% Al–5.4 at.% Ti) [25]. 3D reconstructions of carbon nanotubes in nylon and Si nanoparticles in an Si matrix have been obtained using plasmon excitation in low-loss electron energy loss spectroscopy (EELS) [26, 27] while electron holography was used to characterize the internal electric potential of semiconductor p–n junctions at nm resolution [28]. FIB/SEM slice-and-view can reveal the 3D microstructure of porous materials [29] as well as precipitation morphologies [30], while combinations with electron backscattered diffraction (EBSD) will reveal crystal grain structures in 3D [31]. More examples as well as a step-wise introduction to the theory of electron tomography and reconstruction techniques can be found in the *Handbook of Nanoscopy*, chapter 7, while applications on biomaterials can be found in chapter 36 [32].

In the present paper, some recent results of quantitative 3D EM on structural and functional materials obtained by the authors are reviewed and put in the perspective of existing and potential applications of the investigated systems.

2. Results

2.1. 3D investigations on Ni_4Ti_3 precipitates in Ni–Ti

Near-equiatomic Ni–Ti has been widely studied due to its unique functional properties of shape memory and superelasticity [33, 34]. These phenomena originate from the structural $B2$–$B19'$ martensitic and intermediate R-phase transformations underlying this particular functional behaviour [34]. In alloys trained for practical applications, these properties are controlled by the presence of Ni_4Ti_3 precipitates that can be induced in the austenite $B2$ matrix by a proper thermo-mechanical treatment. The formation of these Ni-rich precipitates allows for a stabilization of the matrix composition by balancing the number and size of the precipitates with the annealing time and temperatures [34]. This stabilization is extremely important since the transition temperatures of the martensitic transformation are strongly dependent on the chemical composition. Moreover, in the case that the precipitate formation has not been completed, concentration gradients remain in the area next to the precipitate and this can again locally influence the onset of the martensitic transformation [35]. However, the strongest impact of the precipitation on the martensitic transformation is the strain field induced in the surrounding matrix due to a shortening of the c-axis and this prepares the matrix for a transformation into the intermediate R-phase [35–37] potentially supported by a stress-induced spatial variation of the concentration [38]. Also, the precipitates are found to be harder than the matrix, so their internal lattice is considered to be unstrained [39]. In view of these features, it is important to investigate not only these local phenomena but also the 3D shapes and distribution of these precipitates.

2.1.1. 3D strain field determination by conventional high-resolution TEM (HRTEM). From conventional TEM observations it is known that well-developed Ni_4Ti_3 precipitates have a lenticular shape with a central plane parallel to the $\{111\}_{B2}$ planes, as seen in figure 2(a) [40]. The combination of ordering and orientation yields eight variants, but since two ordering variants share the same habit plane, only four different orientations are observed in conventional SEM. The precipitates have a rhombohedral atomic structure with $a = 0.670$ nm, $\alpha = 113.9°$ [40] (or $a = b = 1.124$ nm, $c = 0.5077$ nm in the hexagonal description [41]), which has recently been refined by dedicated electron [42] and neutron diffraction to a space group R-3 [43].

The actual size, morphology and distribution of the Ni_4Ti_3 precipitates depend strongly on the thermo-mechanical history of the material. Short- and intermediate-term stress-free ageing can lead to heterogeneous microstructures with precipitates concentrating around grain boundaries (GB), splitting the transformation into several steps upon cooling [44, 45], while compressing or elongating the sample during heating can introduce preferential growth of a single variant [46–48]. Also, the volume fraction of precipitates will influence the overall composition of the matrix, having a strong effect on the martensite transformation temperatures [49]. Moreover, the Ni_4Ti_3 precipitates with heterogeneous microstructures concentrating around GB have drawn increasing interest due to their special contribution to the so-called multistage martensitic transformation, although the mechanism of this phenomenon is still controversial [45, 48, 50–55]. Therefore, the study of the 3D distribution of these precipitates is of importance for a better understanding of their essential influence on the martensitic and R-phase transformations of the $B2$ matrix.

The first quantified 3D-type information regarding these lenticular precipitates was obtained by combining 2D strain gradient data from two independent crystallographic orientations in homogenized polycrystal $Ni_{51}Ti_{49}$ annealed at 723 or 773 K for 4 h [37]. These results were obtained by classic HRTEM imaging in a top-entry LaB_6 JEOL 4000EX and geometric phase analysis (GPA) of the lattice images. In the $[1\,0\,\bar{1}]_{B2}$ viewing direction the precipitate–matrix interface is seen edge-on, while for the $[1\,\bar{1}\,1]_{B2}$ orientation a small overlapping region has to be taken into account. In figure 2(c) the (x, y) reference frame

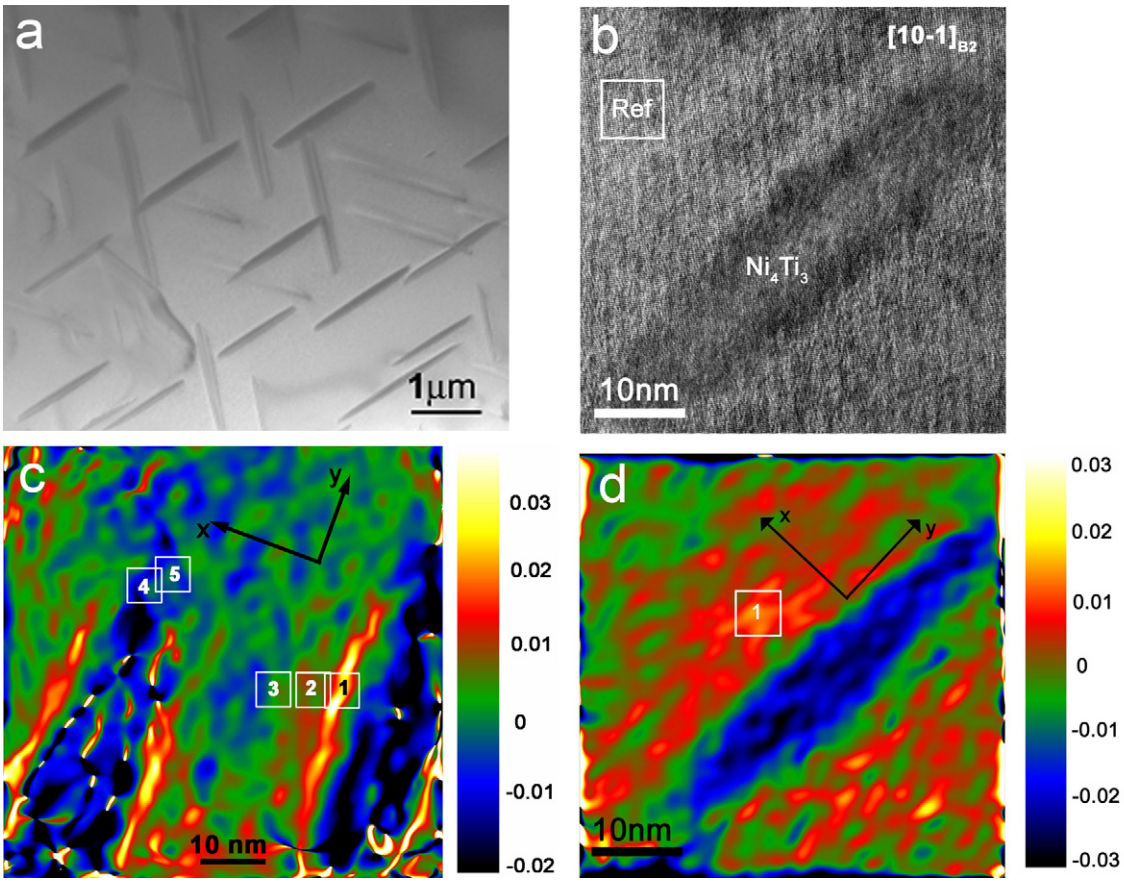

Figure 2. (a) Combination of four orientation variants of Ni_4Ti_3 precipitates in *B*2 austenite, (b) HRTEM $[1\,0\,{-}1]_{B2}$ image of a single precipitate (the square labeled as 'Ref' represents the undistorted austenite matrix), and (c) and (d) GPA maps showing the ε_{xx} matrix strain alongside precipitates observed in $[1\,{-}1\,1]_{B2}$ and $[1\,0\,{-}1]_{B2}$ orientations, respectively ((d) shows the same precipitate as (b)).

corresponds to ($[121]_{B2}$,$[1\,0\,{-}1]_{B2}$), while for figure 2(d) this reference frame is ($[111]_{B2}$,$[1\,{-}2\,1]_{B2}$). Figure 2(b) shows the $[1\,0\,{-}1]_{B2}$ HRTEM image with the results from the GPA analysis for both orientations shown in figures 2(c) and (d) (the numbered squares refer to regions over which the average deformation is measured [37, 41]). When comparing the 2D numerical values measured for the local strains in the matrix with those obtained from a classic Eshelby approach, it was found that the measured strain values are up to ten times larger than the calculated ones and the experimentally observed maximum is located closer to the interface [41]. Although the magnitudes are not the same, the positions of tensile and compressive strain are as expected: compression at the tips and maximum tensile strain along the central axis. Possible differences between the simulation and experiment can be due to the assumptions used for the model, i.e. equal elastic modulus for the precipitate and the matrix and the small deviation of the precipitate shape from the perfect ellipsoid. The latter is clear from conventional TEM (and also from the 3D observations discussed below), while the former corresponds to a shift in low-loss electron spectroscopy intensity, indicating that the precipitates are harder than the matrix [35]. The combination of HRTEM and GPA from these two low index directions yields independent 3D principal strains and directions perfectly matching the transformation strain of a single variant of the *R*-phase, as can be concluded from the values listed in table 1 for area '2' in figure 2(c) [37]. This corresponds well with the observation of *R*-phase nucleation at the Ni_4Ti_3 precipitates [50]. The request for minimization of lattice strain at the secondary interface between the nucleated *R*-phase and austenite matrix can provide the driving force for the formation of a twinned *R*-phase. However, although the match between the 3D numerical values obtained from the GPA measures on the experimental 2D HRTEM images and the *R*-phase deformation is striking, the present approach does not really include a thorough 3D treatment using particular reconstruction algorithms. For example, the mathematical combination of elastic strain values for both the zone axes does not yield structure images along other orientations, as can be expected from a true 3D reconstruction result.

2.1.2. Slice-and-view by FIB/SEM. Although recently a great deal of new results have been reported in 3D electron tomography using TEM, for the present case the size of the precipitates and the respective 3D matrix volumes in which they appear do not really allow for the use of transmission techniques. So, in order to obtain 3D information on shapes and distributions, slice-and-view FIB/SEM was used yielding 3D data sets on cube volumes of around $100\,\mu m^3$ with precipitates having a diameter of the central plane between 50 and 500 nm. For the present results, each sequence

Table 1. 3D measured (E) and calculated ($R1$) principal strains and directions as obtained from the combination of two HRTEM images using GPA and calculated for the transformation of austenite into a single variant of the R-phase, respectively (data for E correspond with the observations at site '2' in figure 2(c)).

	Principal strains			Principal directions		
E	$\begin{pmatrix} -0.0056 & 0 & 0 \\ 0 & -0.0033 & 0 \\ 0 & 0 & 0.0110 \end{pmatrix}$			$\begin{pmatrix} -0.2618 \\ -0.4903 \\ 0.8313 \end{pmatrix}$	$\begin{pmatrix} -0.7553 \\ 0.6403 \\ 0.1398 \end{pmatrix}$	$\begin{pmatrix} 0.6008 \\ 0.5913 \\ 0.5380 \end{pmatrix}$
$R1$	$\begin{pmatrix} -0.0059 & 0 & 0 \\ 0 & -0.0059 & 0 \\ 0 & 0 & 0.0121 \end{pmatrix}$			$\begin{pmatrix} -0.2991 \\ -0.5084 \\ 0.8075 \end{pmatrix}$	$\begin{pmatrix} -0.7598 \\ 0.6389 \\ 0.1209 \end{pmatrix}$	$\begin{pmatrix} 0.5774 \\ 0.5774 \\ 0.5774 \end{pmatrix}$

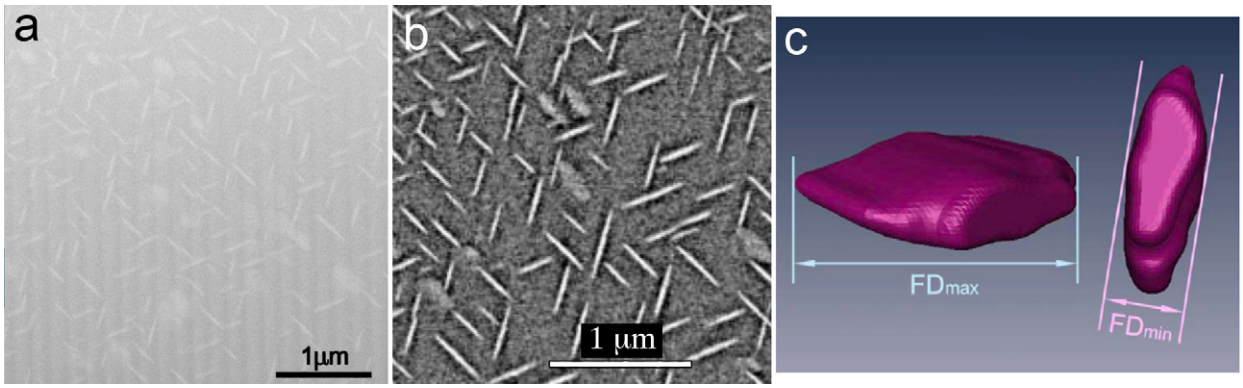

Figure 3. (a) Typical example of an SEM image of Ni_4Ti_3 precipitates showing only limited contrast before image treatment. (b) Better delineated precipitates after image processing. (c) Feret or clip diameter definition (min and max).

contains around 200 2D cross-section images of about $10 \times 5\,\mu m^2$ and obtained at intervals of 25 nm, the image size being further cropped after alignment. A Dual-Beam xT Nova Nanolab 200 FIB/SEM instrument equipped with an automated slice-and-view procedure was used to obtain the series of 2D cross-section images, often overnight.

The sample treatments listed above have been chosen in order to ensure that there are enough precipitates with useful dimensions in any investigated volume. Larger micron-sized precipitates would, of course, be easier to treat, but only a few precipitates would be observed in each selected volume with many of these crossing the volume boundaries. Imaging of smaller nano-sized precipitates would be severely hampered by the slicing procedure. In newer instruments, a smaller Ga^+ beam size can be obtained so that slicing at every 10 nm could be performed allowing the observation of even smaller precipitates.

Due to the similar composition and structure of Ni_4Ti_3 precipitates when compared with the surrounding matrix the most important steps of the image acquisition and optimization relate to the weak contrast of the precipitates, as seen from figure 3(a) [56]. After a careful comparison between different imaging modes, secondary electron (SE) imaging at 5 kV and 1.6 nA was selected with a lateral resolution below 2 nm. For general orientations of the precipitates, no preferential invisibility of particular variants and for a given surface orientation was observed. Of course, it has to be avoided to have the slicing surface normal parallel to a $\langle 111 \rangle$ direction, since this would imply that for one of the variants the precipitate's central plane would also be parallel to the slicing surface by which this variant would be virtually invisible and most of its precipitates would be sliced away.

The obtained 2D SEM images need to be properly processed to improve the image quality in order to ensure the precision of the 3D reconstruction and the following quantitative analysis. First, the image sequences are well aligned, resized (due to the angle between the SEM and FIB beams) and interesting regions are selected. In the present study, due to the so-called 'curtain' artefacts introduced by a low dose of the FIB and a certain heterogeneity in the hardness of the sample [15], a band-pass filter in ImageJ© is applied to suppress those vertical stripe-shaped patterns in the 2D images. Afterwards, a sequence of filters (*wiener2*, *medfilt2*, *imadjust* and *imsubtract*) in Matlab© are applied on the entire sequence of 2D images in order to decrease noise, improve image contrast and remove the gradient background. An example of a cross-section image after image processing is shown in figure 3(b) [56]. The processed image sequences are then segmented in Amira© with the *label field* function to differentiate variants of Ni_4Ti_3 precipitates from each other and from the matrix. The final 3D visualization of the precipitates in the matrix is achieved through the *surfacegen* function in Amira©.

Although the above-presented image processing yields perfectly useful segmented sequences, one needs to be careful with setting the values for the actual parameters involved. Indeed, for example when changing the values for the background subtraction, the width of the precipitates as they finally appear in figure 3(b) can change, eventually leading to the disappearance of a small precipitate or of the shrinking

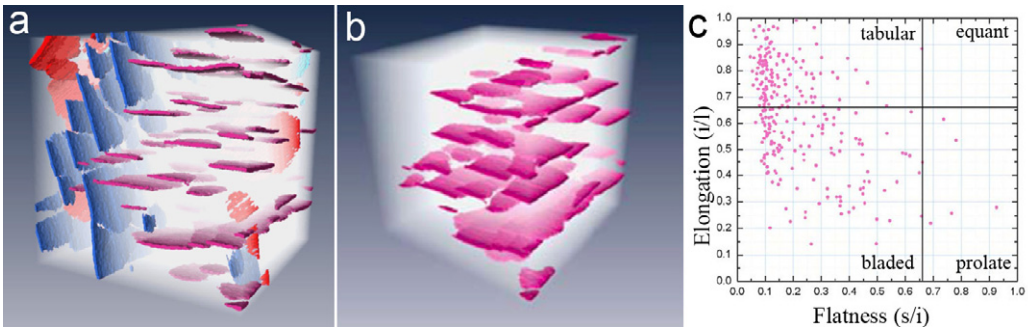

Figure 4. (a) 3D representation of a $5 \times 5 \times 5\,\mu m^3$ volume from a stress-free annealed single crystal, showing groups of single variant precipitates formed by autocatalytic nucleation and growth. (b) A single group selected for ease of visualization. (c) The Zingg and Tucker scheme revealing the shape distribution of the measured precipitates.

of the tip of a larger one. By choosing different sets of extreme values for the parameters in the processing procedure, some boundaries for the precision of the entire procedure could be obtained. After a careful comparison of certain measures obtained directly from the original images and those obtained from processed ones, a precision of about 4% is estimated [56].

From the segmented images, several voxel-based quantitative measures can be obtained for a given precipitate, for example, the volume (V_p), surface area (SA), maximum and minimum Feret or clipper diameter ($FD_{max,min}$) (shown in figure 3(c)) and aspect ratio (AR). The AR is defined as the largest diameter divided by the smallest diameter in the orthogonal plane, the latter two obtained, respectively, from the FD_{max} and FD_{min} clipper estimations of the precipitate disc diameter and thickness [57]. The larger the AR (always $\geqslant 1$) the flatter the precipitate appears. From the measured V_p and SA, the specific surface area (SSA) for each precipitate can be calculated as SA/V_p while the sphericity parameter $\psi\,(\leqslant 1)$ indicates how close the shape is to a sphere ($\psi = 1$). In combination with the remaining matrix or total volume, measures such as volume fraction can then be calculated by combining the data on all precipitates in the respective box.

One should further note that in the case of a precipitate containing an extremely small number of voxels, e.g. below 100, the morphology of the precipitate can no longer correctly be described by the above parameters. This is due to the fact that when the voxel size is comparable to any one of the dimensions of the precipitate, here typically the thickness of the lens shape, the shape of the voxel will strongly influence the bitmap shape of the precipitate and the obtained values for the above parameters. However, in all the cases shown in the following sections, most of the studied precipitates have enough voxel resolution for the present shape and size analysis, with only very few precipitates (<1%) containing too small a number of voxels for a proper analysis, which are then disregarded from the analysis.

Instead of using parameters based on pixel or voxel counting, existing knowledge on the expected shape of the precipitate can further be used for standardizing certain measures. For example, a simulated equivalent ellipsoid with the same principal moments of inertia as the experimentally observed precipitate can be calculated in order to better understand the precipitate morphology and avoid extreme values due to outliers [58]. The different principal axes of this equivalent ellipsoid will be referred to as small (s), intermediate (i) and large (l), the latter two being equal for a perfect lens shape.

The first concrete sample that will be discussed here is the $Ni_{51}Ti_{49}$ single crystal produced using the Bridgman technique, homogenized at 1273 K for 12 h, water quenched and annealed as such (i.e. stress-free) at 823 K for 10 h. Figure 4(a) shows the 3D representation of a sliced box of $5 \times 5 \times 5\,\mu m^3$. Although precipitates belonging to all four variants can be recognized from the numerical data, groups of only three of the variants can be properly distinguished in the image.

Visual inspection of the precipitates belonging to a given variant indicates that they seem to appear in groups, as seen in the example of figure 4(b) where only one variant is retained. As a result, precipitates of the same variant tend to show very few crossings with those belonging to other variants. The phenomenon is attributed to autocatalytic growth [59, 60] in which a new precipitate nucleates in the strain field induced in the matrix by a previously grown precipitate [54, 59]. In total, 129 complete precipitates can be distinguished in the stress-free aged sample, yielding a number density of 1.0 precipitate per cube micron. However, due to the relatively large volume of the single precipitates, the total volume fraction of precipitation in this stress-free case is 6.1%. The precipitates of the stress-free ageing show an average V_p of $0.022\,\mu m^3$ with $SA = 1.11\,\mu m^2$, $FD_{max} = 0.812\,\mu m$, $FD_{min} = 0.113\,\mu m$, $AR = 6.67$ and $\psi = 0.39$ [60].

Based on these quantified 3D data, the precipitation in this stress-free aged sample can be compared with that in a single-crystal sample of the same composition, annealed under the same time and thermal conditions as above but now under a compression of 50 MPa along one of the ⟨111⟩ crystallographic directions of the matrix. Figure 5(a) shows a 3D view of this sample from which it can be concluded that only one variant is retained. From figure 5(b) it is seen that the precipitates are relatively thick, while figure 5(c) shows that some of them tend to coagulate along the plane of their central disc. The investigated box of this sample contains in total 179 complete precipitates, yielding a number density of 2.3 precipitates per cube micron. However, due to the much smaller volume of the present precipitates, the total volume fraction of precipitation in the compressed case is 4.3%,

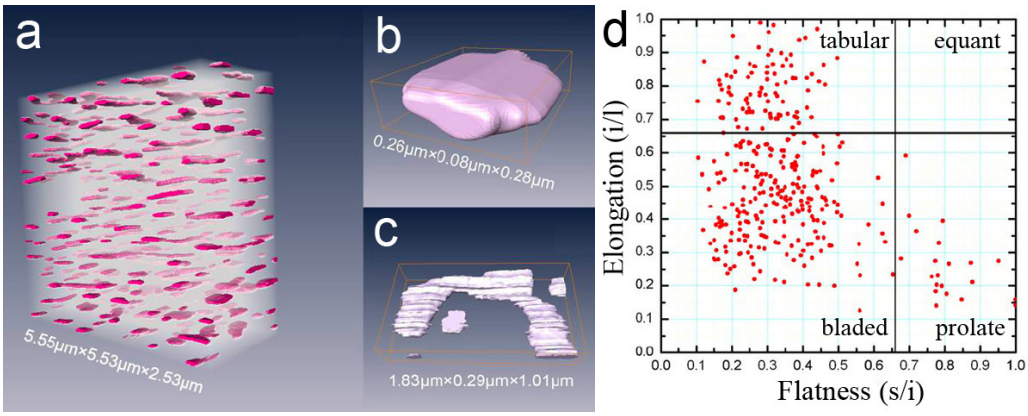

Figure 5. (a) Single variant precipitates as observed in the compressed single crystal. Panels (b) and (c) show relatively thick and coagulated precipitates, which is confirmed by the Zingg and Tucker scheme in (d).

which is substantially smaller than the 4.3% for the stress-free case. The averaged values for the above used parameters for the compressed case are $V_p = 0.0084\ \mu m^3$, $SA = 0.34\ \mu m^2$, $FD_{max} = 0.554\ \mu m$, $FD_{min} = 0.085\ \mu m$, $AR = 6.22$ and $\psi = 0.61$ [61].

When comparing the two Zingg and Tucker schemes [62, 63] shown in figures 4(c) and 5(d), the stress-free aged precipitates are seen to concentrate in the region with extremely flat precipitates, while the compressed precipitates tend to have a higher *s*/*i* ratio, i.e. the latter are essentially thicker. This can be understood from the fact that the external stress during ageing compensates for the internal stress between the precipitates and the matrix in the direction perpendicular to the central plane, and thus promotes the thickening of precipitates. Therefore the precipitates generated from the compressive ageing will have a more cylindrical shape, increasing their sphericity w.r.t. that of the stress-free precipitates. Even more so, as shown in a former study of a polycrystalline $Ni_{50.8}Ti_{49.2}$ sample, the sphericity of a precipitate shows an exponential decrease as the volume increases, which implies that small precipitates tend to have a rounder shape, which can be explained by the classic competition between volume and interface energy. Therefore, it is further understandable that the smaller precipitates generated in the compressive aged sample extend more in the third direction normal to the central disc of the precipitate, while the larger ones in the stress-free aged sample tend to remain very flat [61, 64].

Next to the indicated differences in size and shape, also the interparticle distances and 3D distribution of the precipitates are clearly different between the two samples. With all four variants occurring in large pockets in the stress-free aged sample, a given plate of martensite can be expected to move relatively easily in between a single pocket and parallel to the major surfaces of those lens-shaped precipitates. However, it will be strongly hindered when it arrives at the next pocket of a different variant in which these major surfaces are nearly perpendicular to the preceding martensite plate. Also, by investigating the interparticle distributions in the compressed case a box-like configuration of about 1 μm edge length is observed instead of the expected layered structure [64]. Based on this configuration, the stop-and-go process observed by Michutta *et al* during *in situ* TEM cooling experiments can be better explained [48].

Although the above 3D quantified information on the precipitates is very instrumental in comparing different samples or different thermo-mechanical treatments, the influence of these shapes, sizes, densities, etc on the martensitic transformation, which is the basis for the shape memory and superelastic behaviour, can only be inferred via circumstantial reasoning. An alternative approach is to define appropriate parameters that describe the matrix in between the precipitates and correlate this with the potential development of martensitic plates. One possible approach is to measure the matrix volume available for martensitic transformation based on minimal distances between precipitate images in all 2D slices. In figure 6(a) an example of the search for the largest circles that can be drawn at each given point of the matrix without reaching the surface of the nearest precipitate (or larger circle) is presented. The histogram of these radii, referred to as the matrix distance transform (DT), then yields a measure for the open space of the austenite matrix in between the precipitates. Comparison of this DT parameter for the stress-free and compressed cases (figure 6(b)) shows a more peaked histogram for the latter, indicating less spread in the free matrix zones. Moreover, the precipitates of the stress-free case are spaced further apart and leave more matrix for martensitic transformation than in the compressed case, as seen from substantially larger DT_{mean} and DT_{max} values (230 and 1661 nm compared with 190 and 934 nm for stress-free and compressed samples, respectively) [61]. Also, by using a newly developed water penetration procedure, a kind of percolation function adapted for martensitic transformations, the evolution of a martensitic plate proceeding in the matrix can be simulated. This procedure selects a given pixel of the first row on a given edge of a 2D image and allows it to act as a nucleus for the transformation. In this way it will induce a transformation in some adjacent matrix pixels of the next row, the connected pixels being defined by the opening angle of the resulting cone of transformation. These transformed matrix pixels will again act as nucleation sites for pixels in the next row, etc, thereby continuing the martensite

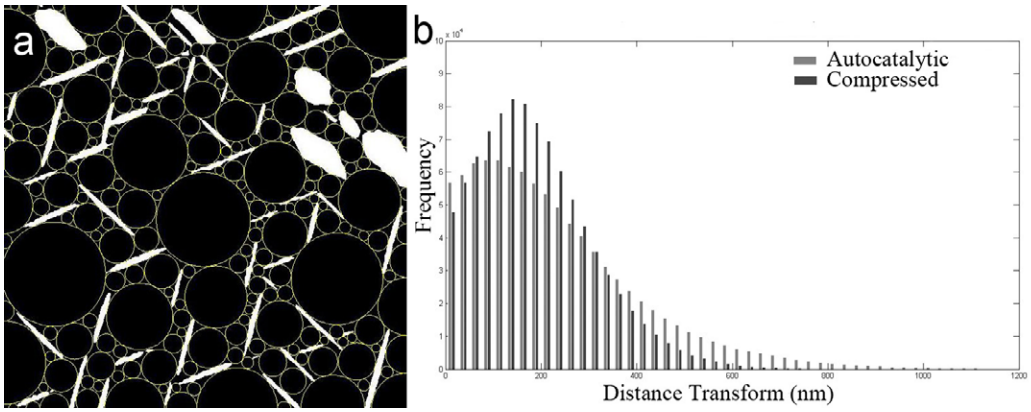

Figure 6. (a) Example of the final circles obtained after the DT transform and (b) histogram of all circle diameters summed over all slices for both stress-free and compressed cases.

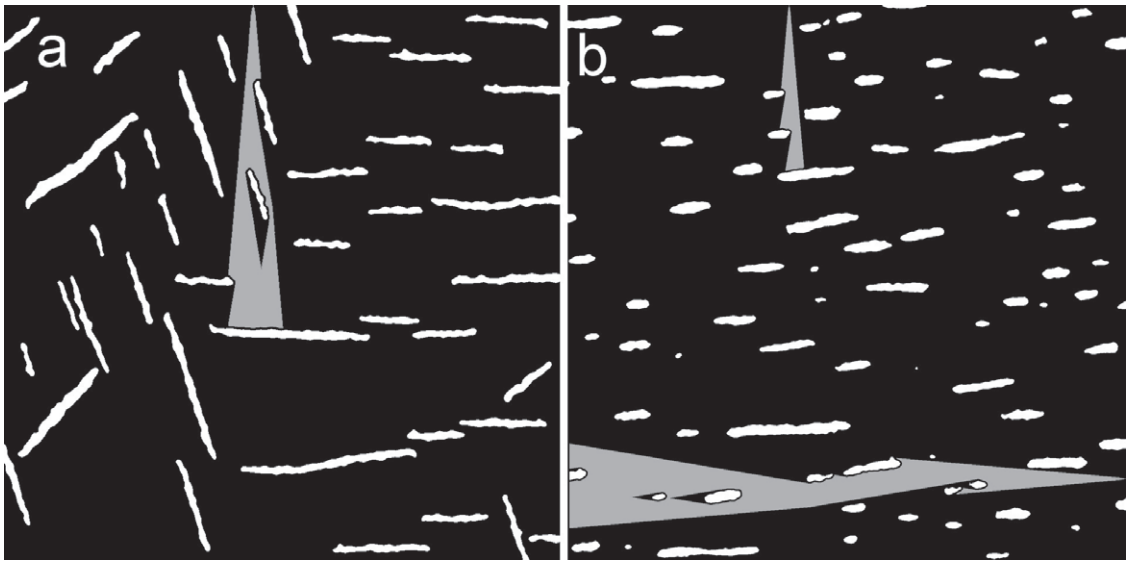

Figure 7. (a) Example of the WP transform (grey) approach for the stress-free and (b) the compressed case, the latter along two perpendicular directions.

plate. If selected pixels in a given row belong to a precipitate, the transformation does not proceed any further through that pixel. In other words, only when the cone extends on one or both sides of a precipitate, can the transformation continue. The result of such a process is seen in figure 7(a) (stress-free case) in which the transformed cone (martensite) is shown in grey, the austenite matrix in black and the precipitates in white. The measured parameter, the filling fraction (FF), is the ratio of the covered transformed area to the area that would be covered if there were no precipitates and is a measure of how easily the transformed area (martensite) can grow in a particular direction. Statistical data are obtained by using all pixels of a given edge row (or column) of all 2D images as a starting set.

In figure 7(b) an example of two cones for the compressed case is given, one parallel and one perpendicular to the precipitate large surfaces (the latter being perpendicular to the ⟨111⟩ compression direction in this sample). From the corresponding histograms of the filling fractions, it is clear that the best condition for a least disturbed transformation path is the direction perpendicular to the compression direction in the compressed sample (figure 7(b)), which yields an FF of 77% [61]. This, of course, is no surprise and confirms the earlier *in situ* work by Michutta *et al* [48]. However, contrary to intuition and to the impression one could get from the single example image of figure 7(a), the next best case is the direction parallel to the compression (FF = 13%) rather than a random ⟨111⟩ direction in the uncompressed single crystal (FF = 6%), although the latter difference remains small certainly when considering the relatively small volume that could be investigated with respect to the autocatalytic pockets. Still, as indicated above, this could be related to the larger size of the precipitates in the stress-free case and especially the different orientations, which naturally set barriers for the martensite growing along different variants. So, although the present two proposals for matrix quantification are only partially 3D, in the sense that they consist of a combination of data from all 2D slices instead of using true measures of the full 3D data (mainly for reasons of calculation time), the results are rather clear and convincing. Still, extending this approach to the full 3D data will probably yield smaller absolute values due to the fact that the effect of precipitates in

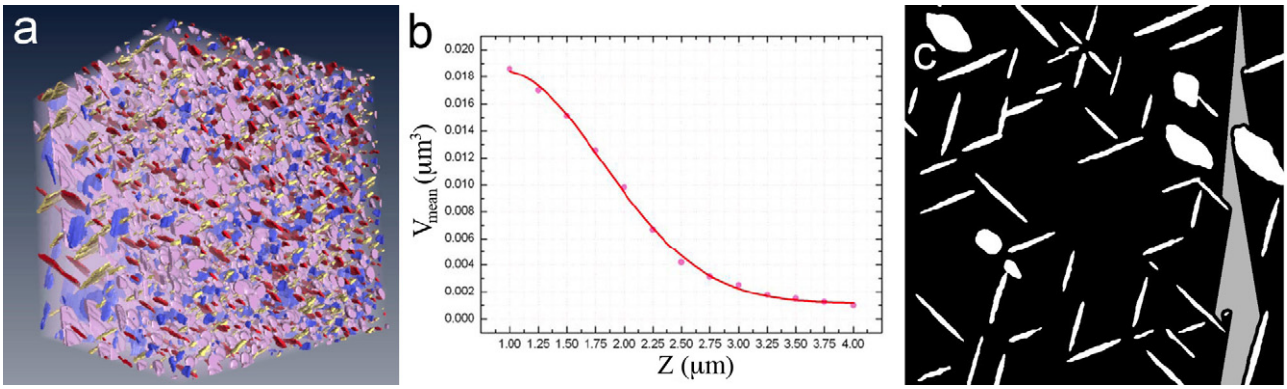

Figure 8. (a) 3D view of a volume close to the grain boundary in the sample exhibiting an MMT. (b) Gaussian trend ($R^2 = 0.998\,55$) of the average precipitate volume when moving from the GI to the GB (dots are experimental measures). (c) WP example for the GI region.

the next slice is at present not taken into account, neither for the DT nor for the FF transforms.

The next type of sample to discuss is a homogenized $Ni_{50.8}Ti_{49.2}$ polycrystal annealed at 773 K for 1 h. In this material, a multiple martensitic transformation (MMT) has been observed and attributed to the differences in precipitate density between regions close to the GB and those in the centre of the grains (grain interior (GI)), the latter being several microns in diameter [44, 45]. For the 3D slice-and-view investigation, a box of $4.75 \times 4.75 \times 4.775\,\mu m^3$ for the GI region and a box of $4.00 \times 4.00 \times 4.00\,\mu m^3$ for the GB region have been selected. In both regions, all four orientation variants of the Ni_4Ti_3 precipitates can be observed. In the GB region, also a part of the intermediate region between the GB and GI is incorporated, as seen in the 3D reconstruction of figure 8(a), which has the GB at the right-front edge of the box showing the smallest precipitates. From both the GI and GB volumes, the same kind of analysis as for the single-crystal samples can be done [58]. To better understand the size evolution of the precipitates in this GB region, the reconstruction box is virtually sliced along the Z direction, i.e. the direction perpendicular to the grain boundary, into small slices of 1 μm thick. By moving this slicing box by steps of 0.25 μm, finally 13 such slices are obtained from the reconstruction volume in the GB region. Then the average volume (V_{mean}) of the precipitates with mass centres in each pocket is calculated. Incomplete precipitates cut by the edge of the full reconstruction volume are not included in this calculation in order to avoid edge-biasing effects from incomplete precipitates. As shown in figure 8(b), the decrease of V_{mean} follows the tail of a Gaussian function when approaching the grain boundary (the position of each data point refers to the center of the virtual slice). The same analysis can be carried out on the average of the central plane diameter FD_{max} for each slice, D_{mean}, which also shows a Gaussian decrease, rather than a linear function as described in [54, 58]. In both cases the R^2 values are above 0.997, indicating a good fit. Moreover, V_{mean} in the first slice, which is closest to the GI region, has a value of $0.0186\,\mu m^3$ while D_{mean} equals 0.854 μm, which are about 26 and 9% lower than the respective average V_p and FD_{max} values in the GI region. The latter indicates that these functions have not yet reached their saturation point at the front side of the GB region and that there will be a slight increase in the 20 μm wide region between the GB and GI regions [58]. As to the shapes of the precipitates, there are more equant- and prolate-shaped Ni_4Ti_3 precipitates in the GB region than in the GI area, which leads to a relatively larger average Ψ for the GB region. These equant- and prolate-shaped precipitates normally have a relatively small volume, which is consistent with growth kinetic simulations showing that the Ni_4Ti_3 precipitates have a sphere shape at the beginning of their growth [46, 65]. Also, the total volume fraction of precipitates is slightly higher close to the GB, which could induce a small concentration difference between the austenite matrices in the centre and at the edge of a grain with an approximately 0.1 at.% excess of Ni for the austenite matrix in the GI region. From a particle distribution function analysis in both regions, it is concluded that the most frequently observed interparticle distance in the GI region, 0.44 μm, is substantially larger than that in the GB region, 0.19 μm, confirming the dense packing of the precipitates close to the grain boundary [58]. Further, no auto-catalytic nucleation and growth has been observed in this sample, possibly due to a larger number of intrinsic nucleation sites when compared with the single-crystal material.

From the water penetration approach shown in figure 8(c), FFs from 4% in the GI volume to only 1% in the GB region (the latter also including part of the intermediate area) are obtained. This implies that the martensitic transformation in the GI region will be less hampered by the packing of precipitates than a transformation close to the grain boundary.

The above quantitative 3D data can be used in order to understand the MMT in the present sample. New evidence has shown that the sequence of multiple transformations in this sample starts at the intermediate region in between the interior and boundary of the grain (i.e. the front part of our GB box), followed by a transformation close to the GB (i.e. the back side of our GB box) after which the GI region transforms. The former two parts include an intermediate R-phase, whereas the GI region directly transforms into martensite [66]. The fact that the GI region transforms at the lowest temperature could be due to the induced concentration difference after the nucleation and growth of the precipitates. Indeed, a higher

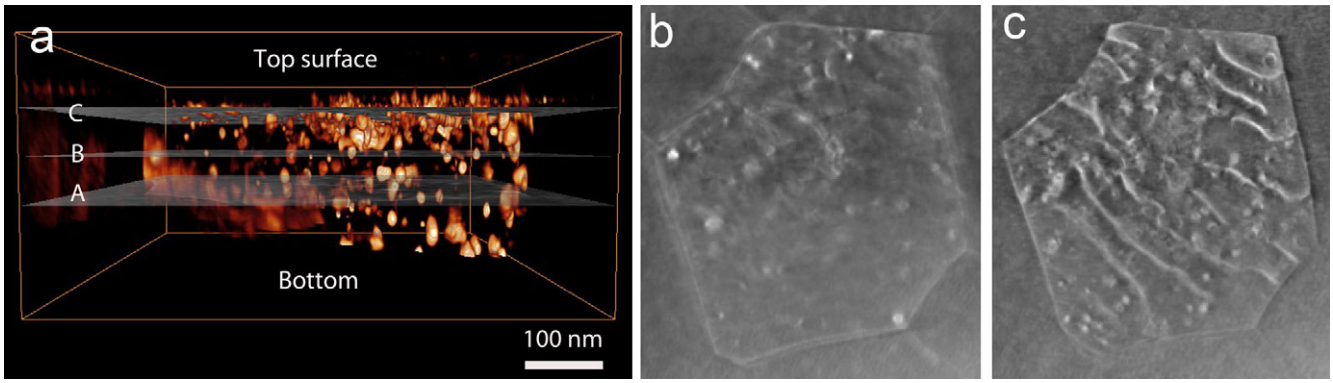

Figure 9. (a) 3D view of Frank dislocation loops in an Al film thinned by FIB (the top and bottom refer to the surface of the FIB cross-section slice); (b) orthoslice in the middle of the sample (slice B in (a)) showing only a few FIB-induced Frank loops; and (c) orthoslice at the top of the sample (slice C in (a)) showing pinning of stress-induced dislocations (long white lines) at FIB-induced Frank loops (white points).

Ni content implies a lower transformation temperature [49] as well as a lower stability range for the *R*-phase [34]. The intermediate region contains semi-coherent precipitates, which act as nucleation centres for the *R*-phase and martensite formation, while there is also sufficient matrix in between the precipitates to allow for a martensitic transformation. This region will thus need a lower driving force and transform first. The region closest to the grain boundary contains many small precipitates close to one another and thus has a conflict of many nucleation sites against only a little matrix to transform and will thus transform after the intermediate region.

2.2. Electron tomography of dislocations in Al nano-beams

In the following example, a high density of Frank dislocation loops was generated in nanocrystalline Al thin films during the preparation of TEM thin foils by FIB thinning. These Al films of 400 nm thickness were deposited on a SiO_2 layer by e-beam evaporation and at a substrate temperature below 150 °C. The mechanical properties of these films are the subject of a series of earlier investigations based on a new nanomechanical on-chip testing method [67] and the films proved to have special mechanical properties such as high ductility. The 3D distribution of the small loops and the dislocations generated in the film due to moderate internal stresses during deposition were obtained using electron tomography in the annular dark-field scanning TEM (ADF-STEM) mode of a Tecnai G2 FEG instrument. These 3D data on dislocation distribution together with information obtained on single dislocations using aberration-corrected high-resolution ADF-STEM were used to investigate the dislocation behaviour as well as the related confined plasticity at the nanoscale in these films [68].

The tomography ADF-STEM tilt series was acquired between –70° and +70° with a 2° interval. Visibility of the dislocations was maintained by satisfying the two-beam $\mathbf{g} = 1\,1\,\bar{1}$ condition over the entire tilt range owing to a special high-angle triple-axis holder (HATA-8075, Mel-Build, Japan, http://www.melbuild.com). Using this two-beam condition both the extrinsic small dislocation loops induced by FIB milling and the intrinsic long dislocations generated during deposition remain visible in all images of the tilt series. The inner angle of the ADF detector used for the tomography experiment was ∼45 mrad, while the 3D volume was reconstructed by a weighted back-projection implemented in the FEI Inspec3D software package. Figure 9(a) shows a 3D reconstruction of dislocations in a single Al grain viewed along the Al thin foil prepared by cross-section FIB. The top and bottom surface labels refer to the FIB slice and are thus, in fact, internal cross-sectional planes of the film with a length of 400 nm. From this 3D view, it is already clear that most of the defects are concentrated at the top surface of the FIB slice, but it is still difficult to distinguish between intrinsic and extrinsic dislocations. The corresponding orthoslices at A, B and C, however, give a clear picture of this difference. Two are shown in figures 9(b) and (c), revealing only extrinsic dislocation loops in the centre of the grain (slice B) and intrinsic dislocation lines being pinned by extrinsic dislocation loops at the surface slice C. Further analysis of the 3D morphology of the long dislocations did not reveal any pronounced cross-slip, which can be explained by the small values of internal stress in the as-deposited Al films, which are thus only very weakly deformed during deposition [68].

2.3. Atomic resolution electron tomography

The physical and chemical properties of nanoparticles are controlled by their 3D morphology, bulk and surface structure and composition. Although 2D atomic-resolution TEM has been feasible for nearly four decades, only recently the step towards true 3D atomic resolution by electron tomography has been taken. Indeed, although the example shown in section 3.1.1 is a unique example of a combination of 2D atomic resolution data, it is not a true 3D reconstruction of a crystalline particle or matrix. The latter has recently been achieved by combining aberration-corrected HAADF-STEM in a double-corrected FEI Titan instrument operating at 80 kV (TEAM0.5), statistical parameter estimation theory and discrete tomography. Unlike for conventional electron tomography, only two atomic resolution images are sufficient for the reconstruction. The latter, however, can only yield reliable data when these images are properly quantified and combined with available knowledge about the particle's

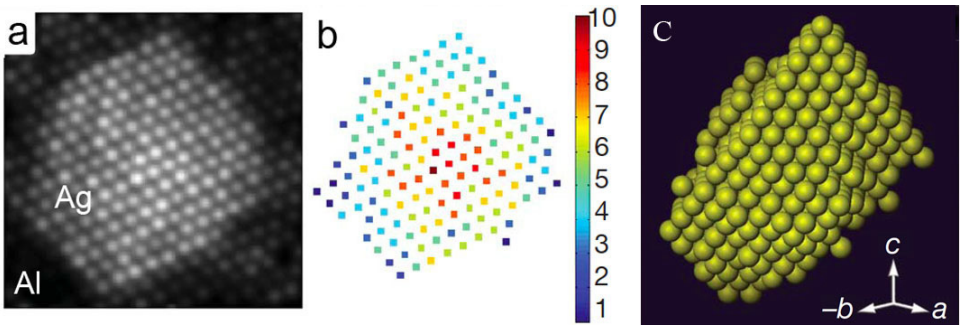

Figure 10. (a) HAADF-STEM image of an Ag particle in an Al matrix viewed along the [10−1] direction; (b) the estimated number of atoms for each column; and (c) [1−10] 3D view of the reconstructed particle based on this and similar data from a ⟨100⟩ direction.

crystallographic structure. Additional projections confirm the reliability of the result.

The applicability of this technique has been shown for an Ag nanoparticle embedded in an Al matrix were the quantification of the number of Ag atoms along a particular crystallographic zone (⟨100⟩ or ⟨110⟩) is based on the intensity of the white dots in the image [13, 69]. This is possible since intensities in a HAADF-STEM image scale with the average atomic number Z, allowing one to distinguish columns containing a certain amount of Ag ($Z = 47$) from pure Al ($Z = 13$) columns when assuming a constant overall thickness of the sample. In figure 10(a) such an embedded Ag particle is shown viewed along a [10−1] direction, while figure 10(b) shows the estimated number of Ag atoms along each column obtained via a model-based statistical parameter estimation procedure [39] in which simulated intensities of a model structure are compared with the measured ones. Based on these atom count results for two different orientations, discrete tomography using *a priori* knowledge such as the fcc-based character of the lattice and the assumption that there are no holes or vacancies yields a full 3D reconstruction seen along the [1−10] direction in figure 10(c). Although this example was chosen as a first model system, it will be clear that atomic resolution data on the morphology of the particle as well as on the interfaces between the particle and the matrix will be of great interest for its influence on the behaviour of this alloy. In subsequent studies, similar results have been reached for stand-alone particles [70].

3. Conclusions

After a short introduction to electron tomography for materials science, the examples presented in this overview clearly show that fundamental research on the 3D structure of functional materials strongly enhances our understanding of the behaviour of these and other materials. Whereas conventional 2D microscopic information at different levels of resolution, of course, has supported the advance of new materials to a great extent, the intrinsic drawbacks related to 2D imaging can be overcome by adding the third dimension via different tools of tomography or sectioning. The revealed possibilities for quantification further allow for a more intrinsic use of these data when coupled to modelling for describing and predicting the behaviour of new systems.

Acknowledgments

We thank G Eggeler and C Somsen of the Rühr-Universität-Bochum (Ge) for the preparation of annealed-compressed Ni–Ti single crystals. M Nishida from Kyushu University (Japan) is acknowledged for the preparation of the polycrystal. The work on Ni–Ti was performed in the frameworks of a European FP6 Project 'Multi-scale modelling and characterization for phase transformations in advanced materials' (MRTN-CT-2004-505226), FWO projects G.0465.05 'The functional properties of SMA: a fundamental approach' and G.0576.09 '3-D characterization of precipitates in Ni–Ti SMA by slice-and-view in a FIB–SEM dual-beam microscope' and a Grant-in-Aid for Scientific Research (B-2036291) from JSPS and an FWO–JSPS Flemish–Japanese collaboration titled 'Advanced techniques for materials characterisation developed by an international cooperation between two centres of electron microscopy for materials research' (VS.007.09N). The thin film work was performed during an IAP programme 'Physics based multilevel mechanics of metals' of the Belgian State Federal Office for Scientific, Technical and Cultural Affairs, under contract no. P6/24. Financial support from the European Union for the Framework 6 programme under a contract for an Integrated Infrastructure Initiative (reference 026019 ESTEEM) is also acknowledged.

References

[1] Lucic V, Förster F and Baumeister W 2005 Structural studies by electron tomography: from cells to molecules *Annu. Rev. Biochem.* **74** 833–65
[2] Hawkes P W 1992b *Electron Tomography: 3D imaging in the TEM* (New York: Plenum)
[3] Midgley P A and Weyland M 2003 3D electron microscopy in the physical sciences: the development of z-contrast and EFTEM tomography *Ultramicroscopy* **96** 413–31
[4] Möbus G, Doole R C and Inkson B J 2003 Spectroscopic electron tomography *Ultramicroscopy* **96** 433–51
[5] Arslan I, Tong J R and Midgley P A 2006 Reducing the missing wedge: high-resolution dual axis tomography of inorganic materials *Ultramicroscopy* **106** 994–1000
[6] Kawase N, Kato M, Nishioka H and Jinnai H 2007 Transmission electron microtomography without the 'missing wedge' for quantitative structural analysis *Ultramicroscopy* **107** 8–15

[7] Biermans E, Molina L, Batenburg K J, Bals S and Van Tendeloo G 2010 Measuring porosity at the nanoscale by quantitative electron tomography *Nano Lett.* **10** 5014

[8] Goris B, Huis M A, Bals S, Zandbergen H W, Manna L and Tendeloo G V 2012 Thermally induced structural and morphological changes of CdSe/CdS octapods *Small* **8** 937–42

[9] Bals S, Batenburg K J, Verbeeck J, Sijbers J and Van Tendeloo G 2007 Quantitative three-dimensional reconstruction of catalyst particles for bamboo-like carbon nanotubes *Nano Lett.* **7** 3669–74

[10] Bals S *et al* 2009 Quantitative three-dimensional modeling of zeotile through discrete electron tomography. *J. Am. Chem. Soc.* **131** 4769–73

[11] Batenburg K J *et al* 2009 3D imaging of nanomaterials by discrete tomography *Ultramicroscopy* **109** 730–40

[12] Jinschek J R, Batenburg K J, Calderon H A, Kilaas R, Radmilovic V and Kisielowski C 2008 3-D reconstruction of the atomic positions in a simulated gold nanocrystal based on discrete tomography: prospects of atomic resolution electron tomography *Ultramicroscopy* **108** 589–604

[13] Van Aert S, Batenburg K J, Rossell M D, Erni R and Van Tendeloo G 2011 Three-dimensional atomic imaging of crystalline nanoparticles *Nature* **470** 374–7

[14] Dunn D N and Hull R 1999 Reconstruction of three-dimensional chemistry and geometry using focused ion beam microscopy *Appl. Phys. Lett.* **75** 3414

[15] Giannuzzi L A and Stevie F A 2004 *Introduction to Focused Ion Beams: Instrumentation, Theory, Techniques and Practice* (New York: Springer)

[16] Groeber M A, Haley B K, Uchic M D, Dimiduk D M and Ghosh S 2006 3D reconstruction and characterization of polycrystalline microstructures using a FIB-SEM system. *Mater. Charact.* **57** 259–73

[17] Holzer L, Muench B, Wegmann M, Gasser P and Flatt R J 2006 FIB-nanotomography of particulate systems: Part I. Particle shape and topology of interfaces *J. Am. Ceram. Soc.* **89** 2577–85

[18] Sakamoto T, Cheng Z, Takahashi M, Owari M and Nihei Y 1998 Development of an ion and electron dual focused beam apparatus for three-dimensional microanalysis *Japan. J. Appl. Phys.* **37** 2051–6

[19] van Benthem K *et al* 2005 Three-dimensional imaging of individual hafnium atoms inside a semiconductor device *Appl. Phys. Lett.* **87** 034104

[20] Xin H L and Muller D A 2009 Prospects for reliable 3D imaging in aberration-corrected STEM, TEM and SCEM *Microsc. Microanal.* **15** 1474–5

[21] Nellist P D, Behan G, Kirkland A I and Hetherington C J D 2006 Confocal operation of a transmission electron microscope with two aberration correctors *Appl. Phys. Lett.* **89** 124105

[22] Takeguchi M, Hashimoto A, Shimojo M, Mitsuishi K and Furuya K 2008 Development of a stage-scanning system for high-resolution confocal STEM *J. Electron Microsc. (Tokyo)* **57** 123–7

[23] Wang P *et al* 2010 Nanoscale energy-filtered scanning confocal electron microscopy using a double-aberration-corrected transmission electron microscope *Phys. Rev. Lett.* **104** 200801

[24] Barnard J S, Sharp J, Tong J R and Midgley P A 2006 High-resolution three-dimensional imaging of dislocations *Science* **313** 319

[25] Hata S *et al* 2008 Electron tomography imaging and analysis of γ' and γ domains in Ni-based superalloys *Adv. Mater.* **20** 1905–9

[26] Gass M H, Koziol K K, Windle A H and Midgley P A 2006 Four-dimensional spectral tomography of carbonaceous nanocomposites *Nano Lett.* **6** 376–9

[27] Yurtsever A, Weyland M and Muller D A 2006 Three-dimensional imaging of nonspherical silicon nanoparticles embedded in silicon oxide by plasmon tomography *Appl. Phys. Lett.* **89** 151920

[28] Wolf D, Lubk A, Lichte H and Friedrich H 2010 Towards automated electron holographic tomography for 3D mapping of electrostatic potentials *Ultramicroscopy* **110** 390–9

[29] Holzer L, Indutnyi F, Gasser P H, Munch B and Wegmann M 2004 Three-dimensional analysis of porous $BaTiO_3$ ceramics using FIB nanotomography *J. Microsc. Oxford* **216** 84–95

[30] Uchic M D, Groeber M A, Dimiduk D M and Simmons J P 2006 3D microstructural characterization of nickel superalloys via serial-sectioning using a dual beam FIB-SEM *Scr. Mater.* **5** 23–8

[31] Zaefferer S and Wright S I 2009 Three-dimensional orientation microscopy by serial sectioning and EBSD-based orientation mapping in a FIB-SEM *Electron Backscatter Diffraction in Materials Science* (Berlin: Springer) pp 109–22

[32] Van Tendeloo G, Van Dyck D and Pennycook S (ed) 2012 *Handbook of Nanoscopy* (Weinheim: Wiley-VCH)

[33] Otsuka K and Wayman M 1998 *Shape Memory Materials* (Cambridge: Cambridge University Press)

[34] Otsuka K and Ren X 2005 Physical metallurgy of Ti–Ni-based shape memory alloys *Prog. Mater. Sci.* **50** 511–678

[35] Yang Z, Tirry W, Lamoen D, Kulkova S and Schryvers D 2008 Electron energy-loss spectroscopy and first-principles calculation studies on a Ni–Ti shape memory alloy *Acta Mater.* **56** 395–404

[36] Madangopal K and Singh J B 2000 A novel B19' martensite in nickel titanium shape memory alloys *Acta Mater.* **48** 1325–44

[37] Tirry W and Schryvers D 2009 Linking a completely three-dimensional nanostrain to a structural transformation eigenstrain *Nature Mater.* **8** 752–7

[38] Zhou N, Shen C, Wagner M F X, Eggeler G, Mills M J and Wang Y 2010 Effect of Ni_4Ti_3 precipitation on martensitic transformation in Ti–Ni *Acta Mater.* **58** 6685–94

[39] Yang Z, Tirry W and Schryvers D 2005 Analytical TEM investigations on concentration gradients surrounding Ni_4Ti_3 precipitates in Ni–Ti shape memory material *Scr. Mater.* **52** 1129–34

[40] Tadaki T, Nakata Y, Shimizu K I and Otsuka K 1986 Crystal structure, composition and morphology of a precipitate in an aged Ti–51 at.% Ni shape memory alloy *Mat. Trans. JIM* **27** 731–40

[41] Tirry W and Schryvers D 2005 Quantitative determination of strain fields around Ni_4Ti_3 precipitates in NiTi *Acta Mater.* **53** 1041–9

[42] Tirry W, Schryvers D, Jorissen K and Lamoen D 2006 Electron-diffraction structure refinement of Ni_4Ti_3 precipitates in $Ni_{52}Ti_{48}$. *Acta Crystallogr.* B **62** 966–71

[43] Khalil-Allafi J, Schmahl W W, Wagner M, Sitepu H, Toebbens D M and Eggeler G 2004 The influence of temperature on lattice parameters of coexisting phases in NiTi shape memory alloys—a neutron diffraction study *Mater. Sci. Eng.* A **378** 161–4

[44] Fujishima K, Nishida M, Morizono Y, Yamaguchi K, Ishiuchi K and Yamamuro T 2006 Effect of heat treatment atmosphere on the multistage martensitic transformation in aged Ni-rich Ti–Ni alloys *Mater. Sci. Eng.* A **438–440** 489–94

[45] Nishida M, Hara T, Ohba T, Yamaguchi K, Tanaka K and Yamauchi K 2003 Experimental consideration of multistage martensitic transformation and precipitation behavior in aged Ni-rich Ti–Ni shape memory alloys *Mater. Trans.* **44** 2631–6

[46] Li D Y and Chen L Q 1997 Shape of a rhombohedral coherent $Ti_{11}Ni_{14}$ precipitate in a cubic matrix and its growth and dissolution during constrained aging *Acta Mater.* **45** 2435–42
[47] Michutta J, Carroll M C, Yawny A, Somsen C, Neuking K and Eggeler G 2004 Martensitic phase transformation in Ni-rich NiTi single crystals with one family of Ni_4Ti_3 precipitates *Mater. Sci. Eng.* A **378** 152–6
[48] Michutta J, Somsen C, Yawny A, Dlouhy A and Eggeler G 2006 Elementary martensitic transformation processes in Ni-rich NiTi single crystals with Ni_4Ti_3 precipitates *Acta Mater.* **54** 3525–42
[49] Tang W 1997 Thermodynamic study of the low-temperature phase B19' and the martensitic transformation in near-equiatomic Ti–Ni shape memory alloys *Metall. Mater. Trans.* A **28** 537–44
[50] Bataillard L, Bidaux J E and Gotthardt R 1998 Interaction between microstructure and multiple-step transformation in binary NiTi alloys using *in-situ* transmission electron microscopy observations *Phil. Mag.* A **78** 327–44
[51] Dlouhy A, Khalil-Allafi J and Eggeler G 2003 Multiple-step martensitic transformations in Ni-rich NiTi alloys—an *in-situ* transmission electron microscopy investigation *Phil. Mag.* **83** 339–63
[52] Fan G, Zhou Y, Chen W, Yang S, Ren X and Otsuka K 2006 Precipitation kinetics of Ti_3Ni_4 in polycrystalline Ni-rich TiNi alloys and its relation to abnormal multi-stage transformation behavior *Mater. Sci. Eng.* A **438–440** 622–6
[53] Khalil Allafi J, Ren X and Eggeler G 2002 The mechanism of multistage martensitic transformations in aged Ni-rich NiTi shape memory alloys *Acta Mater.* **50** 793–803
[54] Khalil-Allafi J, Dlouhy A and Eggeler G 2002 Ni_4Ti_3-precipitation during aging of NiTi shape memory alloys and its influence on martensitic phase transformations *Acta Mater.* **50** 4255–74
[55] Khalil-Allafi J, Eggeler G, Dlouhy A, Schmahl W W and Somsen C 2004 On the influence of heterogeneous precipitation on martensitic transformations in a Ni-rich NiTi shape memory alloy *Mater. Sci. Eng.* A **378** 148–51
[56] Cao S, Tirry W, Van Den Broek W and Schryvers D 2009 Optimization of a FIB/SEM slice-and-view study of the 3D distribution of Ni_4Ti_3 precipitates in Ni-Ti. *J. Microsc.* **233** 61–8
[57] Walton W H 1948 Feret's statistical diameter as a measure of particle size *Nature* **162** 329–30
[58] Cao S, Nishida M and Schryvers D 2011 Quantitative 3D analysis of Ni_4Ti_3 precipitate morphology and distribution in polycrystalline Ni–Ti *Acta Mater.* **59** 1780–9
[59] Kaufman L and Cohen M 1958 Thermodynamics and kinetics of martensitic transformations *Prog. Met. Phys.* **7** 165–246
[60] Perovic V, Purdy G R and Brown L M 1981 Autocatalytic nucleation and elastic stabilization of linear arrays of plate-shaped precipitates *Acta Metal.* **29** 889–902
[61] Cao S, Pourbabak S and Schryvers D 2012 Quantitative 3-D morphologic and distributional study of Ni_4Ti_3 precipitates in a $Ni_{51}Ti_{49}$ single crystal alloy *Scr. Mater.* **66** 650–3
[62] Tucker M E 1985 *Einführung in die sedimentpetrologie* (Stuttgart: Enke Ferdinand)
[63] Zingg T 1935 Beitrag zur schotteranalyse *Schweiz. Mineralogische Petrographische Mitt.* **15** 39–140
[64] Cao S, Somsen C, Croitoru M, Schryvers D and Eggeler G 2010 Focused ion beam/scanning electron microscopy tomography and conventional transmission electron microscopy assessment of. *Scr. Mater.* **62** 399–402
[65] Ke C B, Ma X and Zhang X P 2010 Phase field simulation of growth kinetics of coherent Ni_4Ti_3 precipitate in NiTi shape memory alloy *Acta Metall. Sin.* **46** 84–90
[66] Karbakhsh Ravari B, Kizakibaru N and Nishida M 2012 Quantitative microstructure analyses upon multistage martensitic transformation in an aged Ti–50.8 at.% Ni alloy *J. Alloys Compounds* doi: 10.1016/j.jallcom.2012.03.04
[67] André N *et al* 2007 Multipurpose nanomechanical laboratory revealing the size-dependent strength and ductility of submicron metallic films *Microelectron. Eng.* **84** 2714–8
[68] Idrissi H *et al* 2011 Point defect clusters and dislocations in FIB irradiated nanocrystalline aluminum films: an electron tomography and aberration-corrected high-resolution ADF-STEM study *Microsc. Microanal.* **17** 983–90
[69] Van Aert S, Verbeeck J, Erni R, Bals S, Luysberg M, Van Dyck D and Van Tendeloo G 2009 Quantitative atomic resolution mapping using high-angle annular dark field scanning transmission electron microscopy *Ultramicroscopy* **109** 1236–44
[70] Bals S, Casavola M, van Huis M A, Van Aert S, Batenburg K J, Van Tendeloo G and Vanmaekelbergh D 2011 Three-dimensional atomic imaging of colloidal core–shell nanocrystals *Nano Lett.* **11** 3420–4